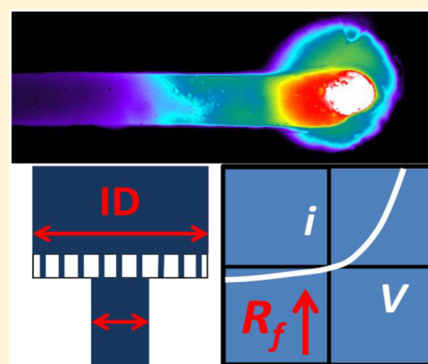


## Controlling the Ionic Current Rectification Factor of a Nanofluidic/Microfluidic Interface with Symmetric Nanocapillary Interconnects

Han Wang,<sup>#</sup> Vishal V. R. Nandigana,<sup>‡</sup> Kyoo Dong Jo,<sup>†</sup> Narayana R. Aluru,<sup>‡</sup> and Aaron T. Timperman<sup>\*,†</sup><sup>†</sup>U.S. Army Corps of Engineers, Construction Engineering Research Laboratory, 2902 Newmark Drive, Champaign, Illinois 61826, United States<sup>#</sup>Department of Chemistry, West Virginia University, Morgantown, West Virginia 26505, United States<sup>‡</sup>Beckman Institute for Advanced Science and Technology, University of Illinois at Urbana–Champaign, Urbana, Illinois 61801, United States

## S Supporting Information

**ABSTRACT:** The current rectification factor can be tailored by changing the degree of asymmetry between the fluid baths on opposite sides of a nanocapillary membrane (NCM). A symmetric device with symmetric fluid baths connected to opposite sides of the NCM did not rectify ionic current; while a NCM connected between fluid baths with a 32-fold difference in cross-sectional area produced a rectification factor of 75. The data suggests that the primary mechanism for the current rectification is the change in cross-sectional area of the fluid baths and the polarity dependent propagation of the enriched and depleted concentration polarization (CP) zones into these regions. An additional contribution to the increasing rectification factor with increasing bath asymmetry appears to be a result of electroconvection in the macropore, with inside diameters (IDs) of 625 and 850- $\mu\text{m}$ . Power spectral density (PSD) analysis reveals chaotic oscillations that are consistent with electroconvection in the  $I$ - $t$  data of the 625 and 850- $\mu\text{m}$  ID macropore devices. In the ON state, current rectification keeps ionic transport toward the NCM high, increasing the speed of processes like sample enrichment. A simple means is provided to fabricate fluidic diodes with tailored current rectification factors.



Ionic current rectification is an important process in the function of biological ion pores, and it can provide enhanced functionality to microfluidic and nanofluidic systems. Ionic current rectification can be used to create diodes for fluidic circuits<sup>1,2</sup> and has been used in analyte enrichment<sup>3–6</sup> and desalination.<sup>7,8</sup> Current rectification produces a greater flow of current in one direction than in the opposite direction, and the current–voltage ( $I$ – $V$ ) plot of a rectifier exhibits a characteristic asymmetric shape. The current rectification factor is the ratio of the forward bias or ON state current to the reverse bias or OFF state current. Ionic current rectification in fluidic systems was initially observed with systems that are asymmetric at the nanoscale. More recently, devices with heterogeneous solutions on opposite sides of a membrane have achieved ionic current rectification using membranes with both nanoscale and microscale pores.<sup>9,10</sup> Current rectification has also been observed in a fluidic system with the symmetric nanochannels filled with a homogeneous solution, providing evidence that current rectification can be achieved without nanoscale asymmetry or the use of heterogeneous solutions.<sup>11</sup>

Conical nanopores are an example of nanofluidic elements with asymmetric geometry that rectify ionic current. Typically, conically shaped pores have a diameter on the nanoscale on the narrow side (the “tip”) and a larger diameter on the wide side (the “base”). For a conical nanopore with a charged surface,

counterion transport is enhanced in the tip to base direction, which forms the current rectification.<sup>12,13</sup> Wei et al. performed pioneering work on ionic current rectification while characterizing ion transport through conical quartz nanopipettes.<sup>14</sup> In addition, asymmetric nanochannels made like funnels also rectify ionic current, and the effect of the taper angle of the nanofluidic funnel to the current rectification ratio has been investigated.<sup>15</sup> Several groups have focused on how to control the current rectification of the conical nanopore. It has been reported that the degree of current rectification can be affected by the diameter of the conical pore, and ionic current rectification increases with decreasing tip diameter.<sup>16</sup> The surface charge inside the nanopore plays a critical role in the ionic current rectification, and the effects of changing the solution have been investigated.<sup>13,17,18</sup> Changing the sign of the surface charge from negative to positive reverses the direction of the current rectification.<sup>19–21</sup> Ali et al. used layer-by-layer deposition of polyelectrolytes into a conical pore to tune the current rectification ratio.<sup>22</sup> In a further refinement, a pH-responsive polymer brush was used to create a rectifier that can be controlled by the solution properties.<sup>23</sup>

Received: May 27, 2014

Accepted: March 13, 2015

Published: March 24, 2015



In addition to using asymmetric geometry, nanochannels with asymmetric surface charge can rectify ionic current and form nanofluidic diodes. Daiguji et al. modeled a nanochannel with asymmetric or discontinuous surface charge and determined that it would perform as a fluidic diode and rectify ionic current.<sup>24</sup> In these devices, ON state currents are produced when a forward-bias produces an ion enriched zone in the nanochannel, and the OFF state currents are produced when a reverse-bias causes formation of an ion depletion zone in the nanochannel. To produce surface charge discontinuity, Karnik et al. modified the nanochannel surface using diffusion limited patterning (DLP). Half of the nanochannel was coated with biotin, which imparts a neutral charge on the surface; while avidin was bound to the other half of the nanochannel, which imparts a positive charge.<sup>25</sup> Yan et al. achieved a discontinuity in surface charge without surface coatings by fabricating  $\text{SiO}_2/\text{Al}_2\text{O}_3$  heterostructured nanotubes to form nanofluidic diodes.<sup>26</sup> In a related approach, photolithography was used to create nanochannels with  $\text{SiO}_2$  and  $\text{Al}_2\text{O}_3$  that had a much sharper charge boundary than the DLP process to create triodes.<sup>27</sup> To actively control the current rectification and ion transport in gated transistors, an external field was applied to change the local surface charge density of the nanofluidic diode.<sup>28–30</sup> For example, Guan et al. introduced a single asymmetrically placed gate electrode or dual split-gate electrodes onto the top of the nanochannel to form the field-effect reconfigurable nanofluidic diodes.<sup>28</sup> Vlassiounk and Siwy used the combination of conical nanopores and differential surface coatings to boost the current rectification factors.<sup>31</sup>

Previously, we reported ionic current rectification in nanofluidic/microfluidic interfaces (NMI) with symmetric nanocapillaries, confirming that ionic current rectification is not exclusively the result of nanoscale asymmetry.<sup>11</sup> In these systems, the fluid baths that the nanocapillaries are connected to are asymmetric in size. Additionally, the ionic permselectivity of the NCM causes concentration polarization (CP) enriched and depleted zones to form on opposite sides of the nanocapillaries. The asymmetry of the fluidic system is proposed to alter the length and stability of the CP depleted and enriched zones. The low current or OFF state is observed when the CP depleted zone is in the micropore, and the high current or ON state is observed when the CP enriched zone is in the micropore.

Although physically distinct, all of these systems produce ionic current rectification by creating a potential barrier that is caused by the formation of a CP ion depleted zone, yielding low off state currents. In the case of the conical nanopores and nanopores with asymmetric surface charge, the asymmetry in the CP depleted zone inside the nanopore produces current rectification, and in NMI devices with asymmetric baths the asymmetry in the CP zone external to the nanocapillaries creates ionic current rectification.

Herein, a simple approach to controlling the current rectification factor of an ionic current rectifier based on a NMI is presented. The asymmetry of the NMI is altered by varying the ID of the larger fluid bath or macropore to produce a simple means to control the current rectification factor. With the experimental conditions used in this work the NCM is ion permselective and induces concentration polarization with its characteristic zones of ion depletion and ion enrichment. If the asymmetry of the depleted and enriched CP zones causes the ionic current rectification, then the current rectification factor is expected to increase with increasing device asymmetry. Two

potential mechanisms for production of ionic current rectification are discussed: changes in the solution resistance based on the changes in cross-sectional area and changes in the suppression of convection from changing the inside diameter of the macropore. Fluorescent microscopy is used to monitor the presence of the depleted or enriched CP zones in the micropore, while the current through the system is recorded as a function of applied voltage. The data provides a new approach to tune the current rectification of NMIs and strengthen the fundamental knowledge of the current rectification mechanism in these devices. It is anticipated that this knowledge will be applied to improve analyte enrichment, ionic purification processes, and the fabrication of simple fluidic diodes.

## ■ EXPERIMENTAL SECTION

**Reagents and Materials.** SU-8 25 photoresist and SU-8 developer were purchased from MicroChem Corp. (Newton, MA). Tridecafluoro-1,1,2,2-tetrahydrooctyl-1-trichlorosilane (United Chemical Technologies, Bristol, PA) was used as a silanizing agent to prevent the PDMS sticking to the surface of the silicon master. Sylgard 184 including PDMS prepolymer and the curing agent was obtained from Dow Corning Corporation (Midland, MI). Silicon wafers with a 10 cm diameter were purchased from Addison Engineering, Inc. (San Jose, CA).

Sodium phosphate electrolyte solution (10 mM, pH 7.2) was made from sodium phosphate monobasic monohydrate (Fisher Scientific, Fair Lawn, New Jersey) and sodium phosphate dibasic heptahydrate (Fisher Scientific Fair Lawn, New Jersey). Ultrapure water nominally dispensed at 18.3 M $\Omega$ -cm was obtained from Barnstead Nanopure Infinity Base Unit (Dubuque, IA). Sodium fluorescein was obtained from Sigma-Aldrich (St. Louis, MO).

The track-etched polycarbonates (TE-PC) NCMs with 10 nm ID pores were obtained from GE Osmonics Inc., Minnetonka, MN, and have a nominal thickness of 6- $\mu\text{m}$ .

**Device Fabrication.** In this study the microfluidic/nanofluidic interfaces were formed by coupling PDMS microfluidic devices with the NCMs that contain the nanocapillaries. Two basic microfluidic designs are used in this work: one is an asymmetric device as shown in Figure 1A, and the other design is symmetric as shown in Figure 1B. The symmetric device has the same vias and microfluidic channels on both sides of the NCM, making it effectively symmetric with a small difference ( $\sim 15\%$ ) in the height of the vertical channels that connect the microchannels with the inlet and outlet. The horizontal microchannels are 100- $\mu\text{m}$  in width and 40- $\mu\text{m}$  in depth, and the vias have a 150- $\mu\text{m}$  ID while extending 60- $\mu\text{m}$  above the microchannel. In this study, the combination of microchannel and the via on the inlet side of the NCM is referred to as the micropore. In the asymmetric design (shown in Figure 1A), the dimensions of the microchannel and vertical via that make up the micropore are the same in all devices on the inlet side of the NCM. However, a series of devices is fabricated with macropores having IDs of 150- $\mu\text{m}$ , 300- $\mu\text{m}$ , 625- $\mu\text{m}$ , and 850- $\mu\text{m}$  and heights of  $\sim 1$  cm. The vias that connect the microfluidic channel ends with the reservoirs have a diameter of 2200- $\mu\text{m}$ .

Standard photolithography and molding processes are used to form the PDMS layers, and the assembly of the NMI devices is shown in Figure S1. The 3D masters, used to form the PDMS layers with microchannels, were fabricated by patterning

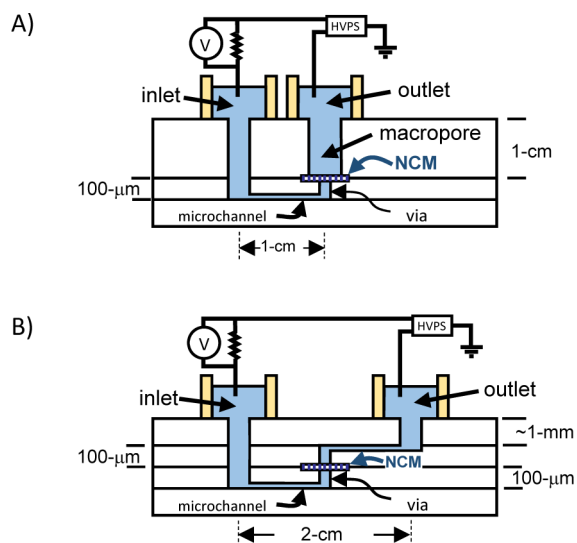


**Figure 1.** Schematics of the asymmetric (A) and symmetric (B) nanofluidic/microfluidic devices are shown. The NCM contains nanocapillaries with 10 nm IDs. Together the microchannel (40- $\mu\text{m}$  height) and the via (60- $\mu\text{m}$  height) are referred to as the micropore. For the asymmetric devices, the macropore IDs are 150, 300, 625, and 850- $\mu\text{m}$ .

SU-8 25 photoresist on a silicon wafer using photolithography. The 3D masters were made with two SU-8 layers that were developed separately. The second SU-8 layer was made by repeating the photolithography process following the completion of first SU-8 layer. The first SU-8 layer forms the horizontal channels, and the second layer forms posts that extend 100- $\mu\text{m}$  above the substrate to create the vias in the PDMS. At first, the photoresist was spin coated at 1000-rpm for 30-s to silicon wafer and prebaked on a hot plate at 90 °C for 20 min. Next, the photoresist coated silicon wafer was covered by the mask, exposed under UV-light (365 nm) for 30-s, and postbaked at 90 °C for 10 min. The first layer was developed by immersing the wafer in SU-8 developer for 3 min. The second layer was begun by spin coating the photoresist at 15-s and prebaked at 90 °C for 2 h. After that, the wafer was cooled to room temperature and exposed under UV-light for 220-s. Next, the coated wafer was developed in SU-8 developer for 6 min. After coating of the two layers photoresist to the wafer, the 3D master is hard baked at 150 °C for 30 min. Then the master surface was treated with tridecafluoro-1,1,2,2-tetrahydrooctyl-1-trichlorosilane under the vacuum for 60 min. Second, the PDMS pieces were molded separately to create the layers shown in Figures 1 and S1. A 10:1 mixture of PDMS prepolymer and the curing agent was degassed in a vacuum desiccator (Bel-art products, Pequannock, New Jersey) to remove all the bubbles and poured to suitable master molds to make PDMS pieces. To make the 100- $\mu\text{m}$  patterned layer of the PDMS (with horizontal channel and 100- $\mu\text{m}$  vertical channels on it), the PDMS mixture on the 3D silicon master was spin coated at 1000-rpm for 30-s and cured on a hot plate at 90 °C for 20 min. The thick top and bottom layers were also made with PDMS using an acrylic machined mold. The thick layers were cured at 70 °C for 2 h. Finally, the top and bottom PDMS pieces were plasma treated using a PDC-32G surface Plasma cleaner (Harrick Scientific, Ossining, NY) for 30-s and irreversibly bonded together with the NCM sandwiched in the middle as shown in Supplementary Figure 1.

**Current Measurements.** Before each current measurement experiment, inlet and outlet reservoir were filled with fresh 10-mM sodium phosphate electrolyte solution at pH 7.2 and degassed in a vacuum desiccator to remove bubbles. Each reservoir was filled with 1 mL phosphate buffer to make solution levels of two reservoirs equal. After each run, the solutions in the reservoirs were tested with pH paper to ensure the pH did not drift. To supply the electrical contact to the microfluidic channel, the platinum electrodes were placed in the reservoirs. In addition, the reservoirs are covered to reduce evaporation. A High Voltage Power Supply (TREK Model 610E) was used to apply potential to each reservoir through a program written by National Instruments Lab Windows/CVI 8.0. There were three voltage programs used in this study: one is for both symmetric and asymmetric devices without the NCM (150, 150, -150, -100, -50, 0, 10, 50, 100, 150 each 5 min); the second is for the symmetric devices with NCM (-150-V, -150-V, -150-V, -150-V, -150-V, -125-V, -100-V, -75-V, -50-V, -10-V, 0-V, 0-V, 150-V, 150-V, 150-V, 150-V, 150-V, 125-V, 100-V, 75-V, 50-V, 10-V each 5 min); the third is for the asymmetric devices with the NCM (similar to the second one except applying voltage at 150-V for 50 min). The longer times were used for larger voltages ( $\pm 150\text{-V}$ ) to ensure sufficient time for the current to reach a quasi-steady state. Both negative voltages and positive voltages in the program were applied to the outlet reservoir. The current through the microfluidic channel was determined by measuring the voltage drop across the 10-k $\Omega$  resistor that was between the inlet reservoir and ground. The voltage was recorded using a digital multimeter (Agilent U1251A, Santa Clara, CA) connected with PC and Agilent GUI Data Logger software. The measured voltage values were converted to current using Ohm's law. The average quasi-steady currents of 5 runs for each voltage were extracted from the current–time ( $I$ - $t$ ) plots to create the current–voltage plots ( $I$ - $V$ ).

The power spectral density was computed using Welch method in Matlab. The current signal is divided into longest possible sections to obtain as close to but not exceed 8 segments, with 50% overlap. Each section is windowed with a Hamming window. The signal is sampled with a sampling frequency ( $f_s$ ) of 1-Hz. The modified periodograms are averaged to obtain the power spectral density (PSD) estimate, for a frequency range  $[0-f_s/2]$ .

The electric field is modeled numerically for the device geometries to quantitatively evaluate the effect of the small degree of asymmetry on the electric field through the system. In the symmetric device, the fluidic regions in the model are the large inlet connecting via, the microchannels, the vias, the NCM, and the large outlet connecting via. In the asymmetric devices, the fluidic regions include the following: the large inlet connecting via, the microchannel, the NCM, and the macropore. The potential ( $\phi$ ) is solved using the Laplace equation without considering the effects of electrophoresis or surface charge. In the present geometry, the NCM porosity is  $6 \times 10^8$  nanopores/ $\text{cm}^2$ , which provides 106 029 nanochannels in fluid conductance. The model is simplified by assuming the same electric field distribution over all the nanochannels and considering only a single nanochannel while adjusting the cross-sectional area of each fluidic section by  $1/106\,029$ . Under these assumptions, the electric potential distribution over the entire system is

$$\nabla^2 \phi = 0 \quad (1)$$



Applying the charge conservation at the walls leads to the following electrostatic boundary condition

$$\mathbf{n} \cdot \nabla \phi = 0 \quad (2)$$

where  $\mathbf{n}$  denotes the unit normal vector (pointing outward) to the wall surface. The voltage  $\phi^{DC}$  (100-V) is applied at the inlet reservoir while the outlet reservoir is grounded as shown in Figure 1. The boundary conditions at the ends of inlet (eq 3) and outlet (eq 4) reservoirs are specified as

$$\phi = \phi^{DC} \quad (3)$$

$$\phi = 0 \quad (4)$$

The equations are solved using the finite volume method in OpenFOAM (Open Field Operation and Manipulation). The Laplacian terms are discretized using second-order central differencing scheme. The details of the solver are discussed in our earlier studies and are independent of grid size.<sup>32–34</sup>

## RESULTS AND DISCUSSION

Current rectification is confirmed in a NMI fabricated with a NCM having symmetric nanocapillaries. The nanocapillaries connect the two larger bath solutions, and current rectification is observed when there is asymmetry in the critical dimension of the baths. For example, current rectification is observed when the nanocapillaries connect a micropore on to a macropore. To study the role of asymmetry in the fluidic system external to the nanocapillaries in the rectification of ionic current, the macropore ID is altered, while the micropore dimensions are held constant. A first control uses an asymmetric microfluidic device with no NCM. This control device provides an Ohmic response, and current rectification is not observed as shown in Figure 2A. In this control device, without the ion permselective NCM, enriched and depleted CP zones are not present. The second control uses a symmetric device with the NCM centered between two identical micropores as shown in Figure 1B. In this case, Figure 2B shows that the current is greatly reduced compared to the system without the ion permselective NCM, as the presence of the NCM results in the formation of depleted CP zone. Although the device is not completely symmetric, it is effectively symmetric, because the regions that the depleted and enriched CP zones extend into are symmetric. The depleted and enriched CP zones do not extend into the reservoirs at the end of the microchannels and consequently the effect of asymmetry in the microchannel-reservoir connections is negligible. Experimentally, the absence of rectification in this device indicates that it behaves as a symmetric device. The results from the computational model of the electric field strength through the devices agree with the experimental observation that the small degree of asymmetry in the symmetric device is negligible. As shown in Table 1, the field strength is the same on opposite sides of the NCM in the symmetric device and different on opposite sides of the NCM in the asymmetric devices. As observed in Figure 2, increasing the macropore diameter increases the current rectification factor. The device with the least degree of asymmetry has a 150- $\mu\text{m}$  ID macropore and yields a rectification factor of 2.8. Although the macropore and via both have an ID of 150- $\mu\text{m}$ , this device is asymmetric because the height of the macropore ( $\sim 1$  cm) is much greater than the height of the via (60- $\mu\text{m}$ ) that forms the entrance to the micropore. As the macropore ID is increased to 300- $\mu\text{m}$ , the rectification factor increases to 6.7,

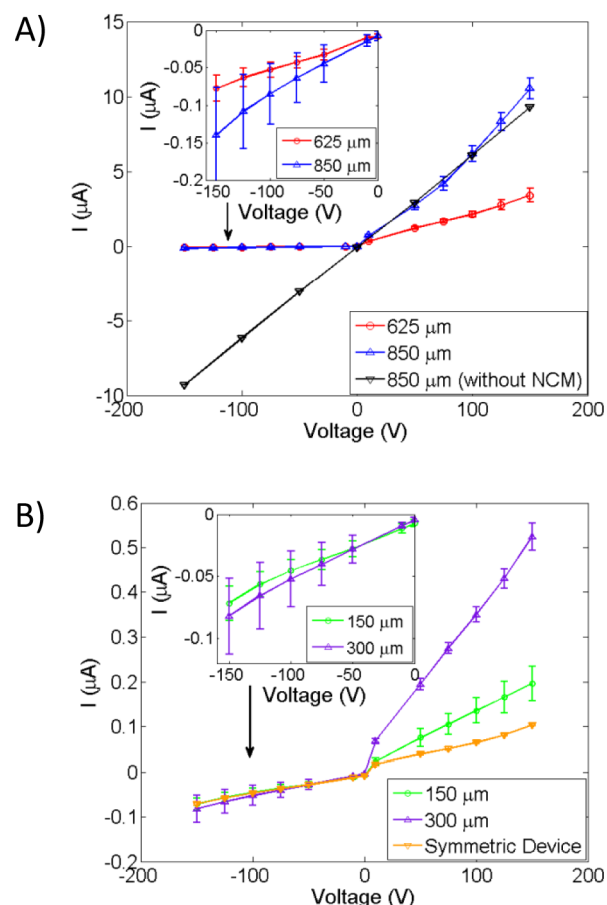


**Figure 2.**  $I$ – $V$  plots for the 625 and 850- $\mu\text{m}$  ID NMI devices and an 850- $\mu\text{m}$  ID device with no NCM are shown in Panel A. The  $I$ – $V$  plots for the symmetric, 150, and 300- $\mu\text{m}$  devices exhibit much lower currents as shown in Panel B.

**Table 1. Computational Results Showing the Electric Field on Both Sides of the NCM in the Symmetric and Asymmetric Devices**

| device             | electric field (V/mm) |          |                      |
|--------------------|-----------------------|----------|----------------------|
|                    | inlet via             | nanopore | outlet via/macropore |
| symmetric          | 2.37                  | 109      | 2.37                 |
| 150- $\mu\text{m}$ | 2.74                  | 126      | 2.75                 |
| 300- $\mu\text{m}$ | 3.16                  | 145      | 1.58                 |
| 625- $\mu\text{m}$ | 3.45                  | 159      | 0.83                 |
| 850- $\mu\text{m}$ | 3.53                  | 162      | 0.62                 |

and as the macropore ID is increased to 625- $\mu\text{m}$  the rectification factor increases to 43. The device with the largest macropore (850- $\mu\text{m}$  ID) produced the largest rectification factor of 75. The data in Table 2 indicates that there is a

**Table 2. Absolute and Relative Changes in the Rectification Factors As a Function of Macropore Cross-Sectional (CS) Area**

| diameter (mm) | CS area (mm <sup>2</sup> ) | rectification factor | $\Delta$ CS area | $\Delta$ rectification factor |
|---------------|----------------------------|----------------------|------------------|-------------------------------|
| 0.150         | 0.018                      | 2.8                  | 1.0              | 1.0                           |
| 0.300         | 0.071                      | 6.7                  | 4.0              | 2.4                           |
| 0.625         | 0.31                       | 43                   | 17               | 15                            |
| 0.850         | 0.57                       | 75                   | 32               | 27                            |

sublinear increase in the rectification factor with increase in the cross-sectional area. The slope of the linear regression analysis shows that the scaling factor is 0.85 and the  $R^2$  value is 0.996. These results indicate that the current rectification factor can be controlled by simply changing the ratio of the micropore and macropore IDs. This novel means to control the current rectification ratio does not require coatings or altering the nanocapillary geometry.

Two mechanisms are likely to contribute to the ionic current rectification, from the asymmetry of the larger macropore system. The data supports the idea that the primary cause of the current rectification is the change in cross-sectional area of the macropore and the resultant effects on the resistance of the depleted and enriched CP zones. Another phenomenon that may contribute to current rectification is electroconvection.

In the present system, three important fluidic regions exist: the micropore, the nanocapillaries, and the macropore. The resistance of each fluidic region is related to its cross-sectional area when it is filled with a homogeneous solution by the following equation:  $R = L/A\sigma$ , where  $R$  is the resistance,  $L$  is the channel or reservoir length,  $A$  is the cross-sectional area, and  $\sigma$  is the conductivity. The different regions of the fluidic system are in series, making the total resistance the sum of the resistances of different fluidic regions. If any region has a very large resistance, its resistance dominates the resistance of the complete system. The application of the voltage to the system causes formation of enriched and depleted CP zones, as ionic current passes through the permselective nanocapillaries. As the depleted and enriched CP zones form, the solution is no longer homogeneous, and the conductivity of each region is also determined by the ions present and their concentration profiles. The ON state or forward bias is observed when the enriched CP zone forms in the micropore as shown in Figure 3A and Figure 3B. In this state, the micropore, which has a high resistance due to its small cross-sectional area and long length, is filled with the enriched CP zone, increasing its conductivity. Conversely, when the polarity is reversed, the depleted CP zone extends into the micropore (as shown in Figure 3C and 3D), resulting in reduced ionic conductivity in the micropore, and consequently the greatly reduced OFF state current is observed. These results support the hypothesis that the change in cross-sectional area and CP induced concentration gradients are the primary cause of ionic current rectification in these devices. The current rectification factors are shown as a function of voltage in Figure 4.

In addition to the changes in the cross-sectional area that effect conductivity, the changes in the macropore ID will also influence convective processes if there are any convective processes present. For the NMI systems presented here, the bulk flow through the macropore is negligible, as only a very small volume of solution flows through the NCM. However, inhomogeneities in the electric field across the NCM surface provide a driving force for convection that is referred to as electroconvection.<sup>35</sup> It is expected that large velocity gradients will exist with high flow through the nanocapillaries that are scattered about the NCM surface that has  $\sim 0.2\%$  porosity. Convection is suppressed by viscous coupling with the solid walls. Although there is no bulk flow through the macropore, the propensity for convection still increases as the macropore ID increases. For a moving solution, the propensity for convection is described by the Reynolds number

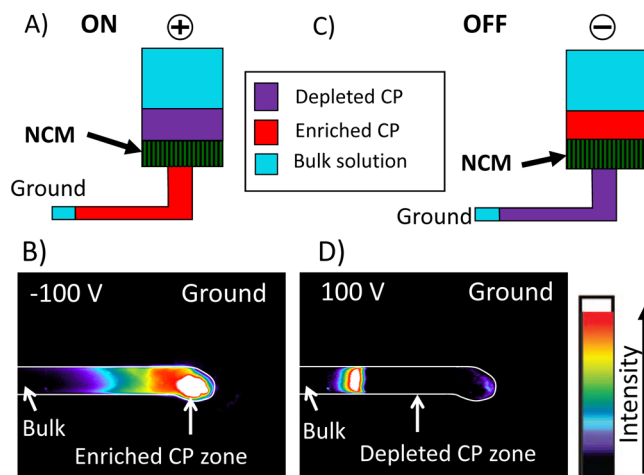


**Figure 3.** Schematics depicting a device (side view) show the location of the depleted and enriched CP zones during the ON (A) and OFF (C) states. The ON state is observed when the enriched CP zone forms in the micropore, and the OFF state is observed when the depleted CP zone forms in the micropore. An inverted fluorescent microscope is used to obtain images (bottom view) of enriched fluorescein in the micropore. In the On state (B), the enriched CP zone forms in the micropore. When the polarity is switched, the depleted CP zone forms in the micropore and the enriched CP zone forms in the macropore and the OFF state is observed. In (D), the depleted CP zone is extending into the micropore with a fluorescein band marking the end of the depleted CP zone. This fluorescein band forms from ions that have vacated the depleted CP zone, and it migrates away from the NCM. The enriched CP zone depicted in (C) is not visible in the fluorescent image (D) because it is outside the field of view and above the PC-NCM. The intensity is encoded by a pseudocolor scale with black representing the lowest fluorescein concentration. The NCMs used in these studies have a negative surface charge and are cation permselective.

$$Re = \frac{d_c \rho \langle v \rangle}{\eta} \quad (5)$$

where  $d_c$  is the channel diameter,  $\rho$  is the fluid density,  $\langle v \rangle$  is the flow velocity, and  $\eta$  is the viscosity. As the Reynolds number increases, the propensity for convection increases and the flow becomes more unstable. In asymmetric NMI systems, the propensity for convection is constant in the micropore, but the propensity for convection increases in the macropore as the macropore ID is increased. If the convection is significant, it will disrupt any concentration gradient (i.e., depleted and enriched CP zones) that forms in that region. Again, convection is expected to be asymmetric and greatest in the macropore. During the ON state, the depleted CP zone forms in the macropore, and increased convection will disrupt the depleted CP zone, making the solution more homogeneous in the macropore. Disruption of the highly resistive CP zone will decrease the resistance of the macropore in a manner similar to removing the largest resistor from a group of resistors connected in series. In contrast, when the system is in the OFF state, the depleted CP zone is in the micropore, where there is no significant change in convection. Consequently, the highly resistive depleted CP zone remains intact and low OFF state currents are observed. Although the enriched CP zone in the macropore is disrupted, it has a negligible effect on the OFF state current, because it is not a current limiting region. It is interesting to note that an overlimiting current is observed with the 850- $\mu\text{m}$  macropore device, which means that the ON state

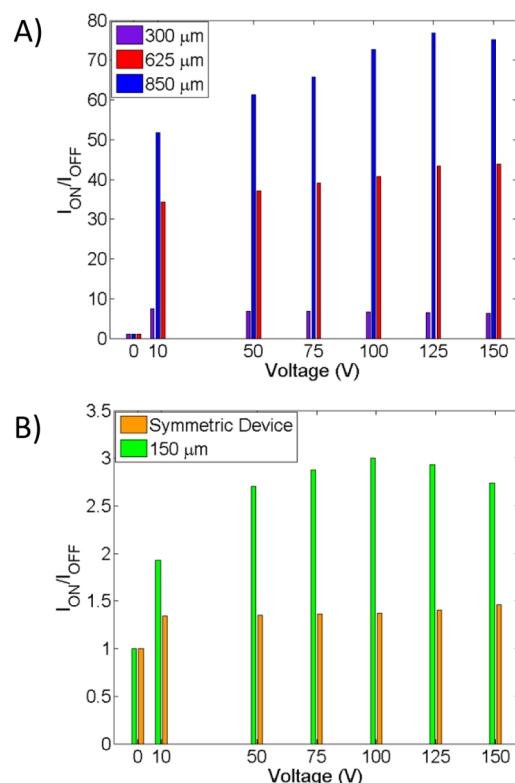


**Figure 4.** Current rectification factors are shown as a function of voltage for (A) 300, 625, and 850- $\mu\text{m}$  macropore devices (b) symmetric and 150- $\mu\text{m}$  macropore devices.

current with the NCM exceeds the current observed with no NCM in the device, as shown in Figure 2A. Geometric effects, the difference in cross-sectional area, cannot create an overlimiting current; therefore, another mechanism must also contribute. All of the  $I$ - $V$  plots for the control devices without an NCM exhibit Ohmic behavior and the currents are similar in value, although the current decreases slightly as the macropore ID decreases. Consequently, the observed trend is that the ON state current approaches and reaches the overlimiting case as the macropore ID is increased. The existence of an overlimiting current is well established when an electric field is applied across a permselective ion exchange membrane.<sup>32</sup>

Noise produced by electroconvection is typically chaotic in nature and gives rise to lower frequency current oscillations.<sup>35</sup> The energy/power spectrum of such chaotic signals usually depicts a  $1/f$  scaling. Similarly, fluctuations in fluid transfer through nanocapillaries are known to cause  $1/f$  noise.<sup>35</sup> Highly chaotic oscillations are present in the current signal in the ON state for 625- $\mu\text{m}$  and 850- $\mu\text{m}$  ID macropores, while little noise was observed for smaller ID macropores at an applied voltage of 150-V. Also, the magnitude of the noise in the OFF state is not as significant at any reservoir diameter, compared to its ON state counterpart. We believe these observations indicate that it is probable that electroconvection contributes to the high rectification factors observed in the 625 and 850- $\mu\text{m}$  ID devices. The dynamics of the fluctuating current are apparent in the  $I$ - $t$  plots, and characteristic segments of the  $I$ - $t$  plots are shown in Supplementary Figure 2.

In our system, the power spectral density analysis revealed no interesting scaling for the OFF state as shown in Figure 5A. In the ON state, for frequencies between 0.01 to 0.05-Hz, we observed only Brownian type noise spectra as the power

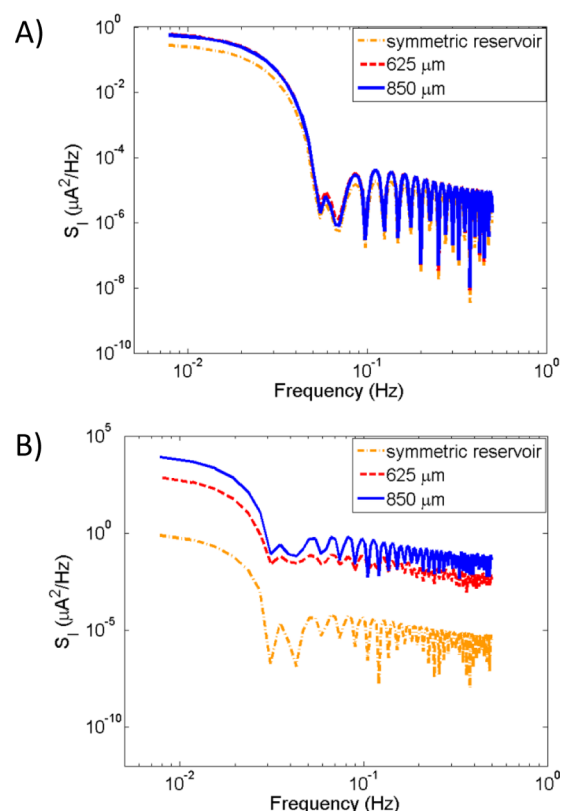


**Figure 5.** Noise in the current signal as a function of frequency is characterized using power spectra density (PSD) plots, for both (A) the OFF and (B) ON states at an applied voltage, 150-V.

spectral density scales approximately as  $1/f^{2.2}$  as shown in Figure 5B. The low data acquisition rate (1-Hz) prevents analysis of the spectral density above 1-Hz, as it leads to signal attenuation. In spite of this constraint, in the frequency range between 0.0938-Hz and 0.4258-Hz, PSD analysis revealed  $1/f^{0.81}$  type scaling for 850  $\mu\text{m}$  device (as shown in Figure 6),  $1/f^{1.18}$  for 625  $\mu\text{m}$ ,  $1/f^{1.61}$  for 300  $\mu\text{m}$ ,  $1/f^{1.55}$  for 150  $\mu\text{m}$ , and  $1/f^{1.59}$  for the symmetric device (as shown in supplementary Figure 3). The scaling factors near one for large macropore diameters in the ON state are strong indicators of chaotic oscillations that are consistent with electroconvection.<sup>36</sup> Likewise, the scaling factors between 1.5 and 2.0 are consistent

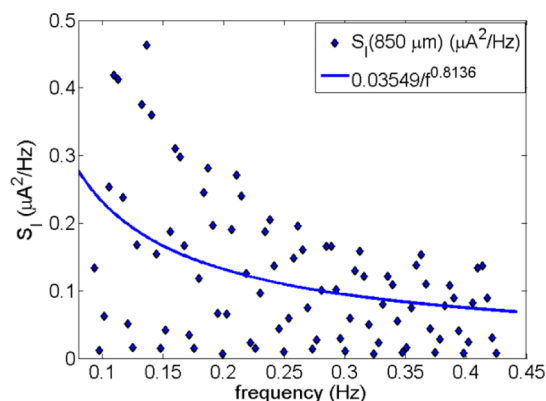


**Figure 6.** PSD fitting for the 850- $\mu\text{m}$  device at 150-V ON state is shown with  $1/\text{frequency}$  scaling. Some white noise is present that does not scale as a function of frequency.



with thermal/Brownian dynamics.<sup>37</sup> Therefore, the spectral density analysis of the noise is consistent with the hypothesis that electroconvection is present in the devices with larger macropores, although other processes, such as water splitting and fluctuations in nanopore surface charge, are known to also produce chaotic oscillations. Druzgalski et al. modeled electroconvection at the interface between a permselective material and bulk solution and found that chaotic instabilities could create multilayer vortices that can disrupt the depleted and enriched CP zones.<sup>36</sup> Siwy and co-workers have investigated the noise through single conical nanopores and concluded that noise characteristics were not of the type created by vortices within the nanopores or by disruption of surface charge. Water splitting has also been suggested as a potential mechanism for generation of the chaotic noise in single nanopore systems.<sup>38</sup> The asymmetric NMI devices presented in this paper are not single nanopore devices and have ~500,000 nanopores or nanocapillaries in the 150- $\mu\text{m}$  area defined by the vertical via of the micropore, making the noise fluctuations an ensemble average of the current through these pores.

## CONCLUSIONS

The current rectification factor can be tailored by controlling the asymmetry ratio between the reservoir baths that are connected to opposite sides of a NCM. As the asymmetry ratio of the micropore and macropore increases, the current rectification factor of the device increases as well. Therefore, the asymmetry ratio can be used to fabricate devices with specific rectification factors. The current rectification is a result of the polarity dependent extension of the CP depleted zones into the fluidic regions with different cross-sectional areas and critical dimensions. Chaotic oscillations in the measured current of the 625- $\mu\text{m}$  and 850- $\mu\text{m}$  devices are consistent with the idea that electroconvection can contribute to the current rectification as well. These current oscillations are not significantly observed in the devices with 150- $\mu\text{m}$  and 300- $\mu\text{m}$  macropore IDs. However, current rectification is still present in the devices with 150- $\mu\text{m}$  and 300- $\mu\text{m}$  macropore IDs, indicating that the geometric asymmetry is the primary mechanism. Future experiments will aim at direct measurements of convection in the macropore and decoupling the contributions of the different mechanisms.

## ASSOCIATED CONTENT

### Supporting Information

Three additional figures are available that show details of device fabrication, representative baseline noise for OFF and ON states, and PSD analysis of baseline noise from the 625- $\mu\text{m}$ , 300- $\mu\text{m}$ , 150- $\mu\text{m}$ , and symmetric devices. This material is available free of charge via the Internet at <http://pubs.acs.org>.

## AUTHOR INFORMATION

### Corresponding Author

\*E-mail: [aaron.timperman@usace.army.mil](mailto:aaron.timperman@usace.army.mil)

### Notes

The authors declare no competing financial interest.

## ACKNOWLEDGMENTS

This publication represents research that was funded by the U.S. Army Environmental Quality and Installations Basic Research Program.

## REFERENCES

- (1) Maglia, G.; Heron, A. J.; Hwang, W. L.; Holden, M. A.; Mikhailova, E.; Li, Q.; Cheley, S.; Bayley, H. *Nat. Nanotechnol.* **2009**, *4*, 437–440.
- (2) Groisman, A.; Enzelberger, M.; Quake, S. R. *Science (Washington, DC, U. S.)* **2003**, *300*, 955–958.
- (3) Wang, Y.-C.; Stevens, A. L.; Han, J. *Anal. Chem.* **2005**, *77*, 4293–4299.
- (4) Pu, Q.; Yun, J.; Temkin, H.; Liu, S. *Nano Lett.* **2004**, *4*, 1099–1103.
- (5) Kelly, K. C.; Miller, S. A.; Timperman, A. T. *Anal. Chem.* **2009**, *81*, 732–738.
- (6) Zhang, Y.; Timperman, A. T. *Analyst* **2003**, *128*, 537–542.
- (7) Kim, S. J.; Ko, S. H.; Kang, K. H.; Han, J. *Nat. Nanotechnol.* **2010**, *5*, 297–301.
- (8) Prakash, S.; Lucido, J.; Georgiadis, J. G.; Shannon, M. A. *Abstracts of Papers, 233rd ACS National Meeting, Chicago, IL, United States, March 25–29, 2007* 2007, SUST-113.
- (9) Cheng, L.-J.; Guo, L. J. *Nano Lett.* **2007**, *7*, 3165–3171.
- (10) Yuskov, E. C.; An, R.; Mayer, M. *ACS Nano* **2010**, *4*, 477–487.
- (11) Miller, S. A.; Kelly, K. C.; Timperman, A. T. *Lab Chip* **2008**, *8*, 1729–1732.
- (12) Apel, P. Y.; Korchev, Y. E.; Siwy, Z.; Spohr, R.; Yoshida, M. *Nucl. Instrum. Methods Phys. Res., Sect. B* **2001**, *184*, 337–346.
- (13) Siwy, Z.; Fulinski, A. *Phys. Rev. Lett.* **2002**, *89*, 198103/198101–198103/198104.
- (14) Wei, C.; Bard, A. J.; Feldberg, S. W. *Anal. Chem.* **1997**, *69*, 4627–4633.
- (15) Perry, J. M.; Zhou, K.; Harms, Z. D.; Jacobson, S. C. *ACS Nano* **2010**, *4*, 3897–3902.
- (16) Kovarik, M. L.; Zhou, K.; Jacobson, S. C. *J. Phys. Chem. B* **2009**, *113*, 15960–15966.
- (17) Siwy, Z.; Apel, P.; Baur, D.; Dobrev, D. D.; Korchev, Y. E.; Neumann, R.; Spohr, R.; Trautmann, C.; Voss, K.-O. *Surf. Sci.* **2003**, *532–535*, 1061–1066.
- (18) Siwy, Z.; Apel, P.; Dobrev, D.; Neumann, R.; Spohr, R.; Trautmann, C.; Voss, K. *Nucl. Instrum. Methods Phys. Res., Sect. B* **2003**, *208*, 143–148.
- (19) Siwy, Z.; Heins, E.; Harrell, C. C.; Kohli, P.; Martin, C. R. *J. Am. Chem. Soc.* **2004**, *126*, 10850–10851.
- (20) He, Y.; Gillespie, D.; Boda, D.; Vlassioulak, I.; Eisenberg, R. S.; Siwy, Z. S. *J. Am. Chem. Soc.* **2009**, *131*, 5194–5202.
- (21) Umehara, S.; Pourmand, N.; Webb, C. D.; Davis, R. W.; Yasuda, K.; Karhanek, M. *Nano Lett.* **2006**, *6*, 2486–2492.
- (22) Ali, M.; Yameen, B.; Cervera, J.; Ramirez, P.; Neumann, R.; Ensinger, W.; Knoll, W.; Azzaroni, O. *J. Am. Chem. Soc.* **2010**, *132*, 8338–8348.
- (23) Yameen, B.; Ali, M.; Neumann, R.; Ensinger, W.; Knoll, W.; Azzaroni, O. *J. Am. Chem. Soc.* **2009**, *131*, 2070–2071.
- (24) Daiguji, H.; Oka, Y.; Shirono, K. *Nano Lett.* **2005**, *5*, 2274–2280.
- (25) Karnik, R.; Duan, C.; Castelino, K.; Daiguji, H.; Majumdar, A. *Nano Lett.* **2007**, *7*, 547–551.
- (26) Yan, R.; Liang, W.; Fan, R.; Yang, P. *Nano Lett.* **2009**, *9*, 3820–3825.
- (27) Cheng, L.-J.; Guo, L. J. *ACS Nano* **2009**, *3*, 575–584.
- (28) Guan, W.; Fan, R.; Reed, M. A. *Nat. Commun.* **2011**, *2*, 1514/1511–1514/1518.
- (29) Kalman, E. B.; Sudre, O.; Vlassioulak, I.; Siwy, Z. S. *Anal. Bioanal. Chem.* **2009**, *394*, 413–419.
- (30) Karnik, R.; Fan, R.; Yue, M.; Li, D.; Yang, P.; Majumdar, A. *Nano Lett.* **2005**, *5*, 943–948.
- (31) Vlassioulak, I.; Siwy, Z. S. *Nano Lett.* **2007**, *7*, 552–556.
- (32) Nandigana, V. V. R.; Aluru, N. R. *J. Colloid Interface Sci.* **2012**, *384*, 162–171.
- (33) Nandigana, V. V. R.; Aluru, N. R. *Electrochim. Acta* **2013**, *105*, 514–523.
- (34) Nandigana, V. V. R.; Aluru, N. R. *J. Fluids Eng.* **2013**, *135*, 021201 DOI: 10.1115/1.4023442.

- (35) Rubinstein, I.; Zaltzman, B. *Phys. Rev. E: Stat. Phys., Plasmas, Fluids, Relat. Interdiscip. Top.* **2000**, *62*, 2238–2251.
- (36) Druzgalski, C. L.; Andersen, M. B.; Mani, A. *Phys. Fluids* **2013**, *25*, 110804/110801–110804/110817.
- (37) Voss, R. F. In *33rd Annual Symposium on Frequency Control*. 1979, 1979; pp 40–46.
- (38) Powell, M. R.; Sa, N.; Davenport, M.; Healy, K.; Vassiouk, I.; Letant, S. E.; Baker, L. A.; Siwy, Z. S. *J. Phys. Chem. C* **2011**, *115*, 8775–8783.